Energy Advances

ROYAL SOCIETY OF CHEMISTRY

PAPER

View Article Online
View Journal | View Issue

Check for updates

Cite this: *Energy Adv.*, 2023, 2, 1399

Alkylated Y-series acceptors for ternary organic solar cells with improved open-circuit voltage processed from non-halogenated solvents†

Peter Fürk, [a] David Paarhammer,[a] Igors Klimenkovs, [b] Andrejs Savkins, [b] Kristaps Berzins,[b] Matiss Reinfelds, [a] Jana B. Schaubeder, [c] Heinz Amenitsch, [d] Thomas Rath *[ae] and Gregor Trimmel *[a]

The efficiencies of organic solar cells have steadily increased over the last few decades. Recently, other crucial factors have moved into focus, such as the removal of environmentally harmful halogenated solvents. The polymer:acceptor combination **PM6**:**DTY6** has already achieved exceptional efficiencies processed from *o*-xylene. In this work, we focus on improving the efficiency of the promising **PM6**:**DTY6** setup by increasing the photovoltage in a ternary solar cell setup. For this, we synthesized four Y-series acceptors (**Y-Me**, **Y-Pr**, **Y-Bu**, and **Y-Hex**), in which the electron withdrawing fluorine atoms in the end groups were substituted with alkyl chains of increasing length (methyl, propyl, butyl, and hexyl). All four acceptors exhibit upshifted energy levels compared to **DTY6** as well as improved solubility in *o*-xylene with increasing alkyl chain length. The third component successfully increased the open-circuit voltage (V_{OC}) from 0.81 V for the binary reference setup (**PM6**:**DTY6**) to 0.87 V for the ternary setups (**PM6**:**DTY6**:**A**, using 15–20 wt.% of **Y-Me**, **Y-Pr**, **Y-Bu**, and **Y-Hex**, respectively). This resulted in an increase in efficiency from 13.3 ± 0.2% for the binary to 14.1 ± 0.2% for the ternary **PM6**:**DTY6**:**Y-Me** devices. Morphological investigations revealed that the alkylated acceptors facilitate the formation of favourable fibrillar crystals and in addition, they distinctly influence the packing behaviour of the **DTY6** acceptor.

Received 13th April 2023,
Accepted 12th July 2023

DOI: 10.1039/d3ya00163f

rsc.li/energy-advances

Open Access Article. Published on 01 2023. Downloaded on 29/07/25 02:51:43.
This article is licensed under a Creative Commons Attribution 3.0 Unported Licence.

Introduction

Organic solar cells (OSCs) are a promising technology for sustainable energy conversion with continuously increasing power conversion efficiencies (PCEs).[1–3] Recently, through the introduction of the high-performing Y-series acceptors, the PCEs have improved to over 19%.[4–6] With the efficiencies reaching values where OSCs become increasingly attractive for large-scale industrial fabrication, other factors are moving into the spotlight. The replacement of toxic and environmentally harmful halogenated solvents (such as chloroform and chlorobenzene) in the fabrication process is one of them.[7–9] Within the Y-series family, a promising member for processing from non-halogenated solvents is the acceptor **DTY6**, which was introduced by Dong *et al.* in 2020.[10] With longer alkyl side chains in the molecule center, they significantly improved the solubility and achieved an excellent PCE of 16.1% combined with the donor polymer **PM6** (Scheme 1), when processed from *o*-xylene (compared to 10.8% for **PM6**:Y6).

While OSCs based on Y-series acceptors exhibit exceptional short-circuit current densities (J_{SC}) and fill factors (FF), the limiting factor for the PCE is often a moderate open-circuit voltage (V_{OC}), with values around 0.8 V.[11,12] A potent strategy to raise the V_{OC} without sacrificing J_{SC} or FF is the implementation of a second acceptor with shifted frontier molecular orbital (FMO) energies. With careful material design and material matching, these ternary OSCs can find the delicate balance between maximum voltage and maximum current that is necessary for high efficiency solar cells. Because of its potential, many examples have been reported in the literature.[13,14] More specifically, the ternary strategy has also already been applied to Y-series OSCs.[15–21] For example, in 2020, Zhan *et al.* added a

[a] *Institute for Chemistry and Technology of Materials (ICTM), NAWI Graz, Graz University of Technology, Stremayrgasse 9, 8010 Graz, Austria. E-mail: thomas.rath@tugraz.at, gregor.trimmel@tugraz.at*
[b] *Faculty of Chemistry, University of Latvia, Jelgavas 1, Riga, LV-1004, Latvia*
[c] *Institute of Bioproducts and Paper Technology (BPTI), Graz University of Technology, Inffeldgasse 23, 8010 Graz, Austria*
[d] *Institute of Inorganic Chemistry, NAWI Graz, Graz University of Technology, Stremayrgasse 9, 8010 Graz, Austria*
[e] *Joanneum Research, MATERIALS – Institute for Sensors, Photonics and Manufacturing Technologies, Franz-Pichler Straße 30, 8160 Weiz, Austria*

† Electronic supplementary information (ESI) available. See DOI: https://doi.org/10.1039/d3ya00163f

© 2023 The Author(s). Published by the Royal Society of Chemistry

Open Access Article. Published on 01 2023. Downloaded on 29/07/25 02:51:43.
This article is licensed under a Creative Commons Attribution 3.0 Unported Licence.

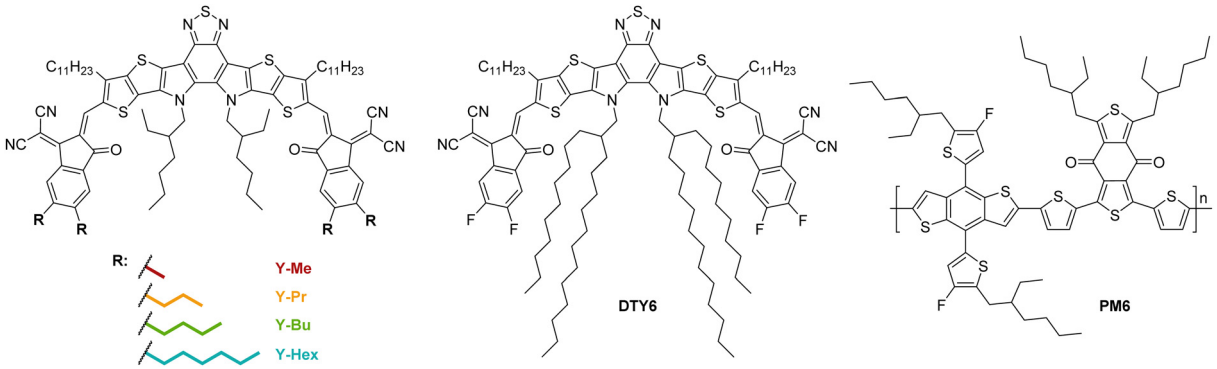

Scheme 1 Molecular structure of the acceptors **Y-Me**, **Y-Pr**, **Y-Bu** and **Y-Hex**, the acceptor **DTY6**, and the donor polymer **PM6**.

single methylated Y-series acceptor (BTP-M) as the third component to **PM6**:Y6.[22] That way, they simultaneously increased the V_{OC} and J_{SC}, resulting in an improved PCE of 17.03% processed from chloroform.

In this work, we apply the ternary OSC approach to the green solvent processable system **PM6:DTY6**. For that, we prepared four Y-series acceptors **Y-Me**, **Y-Pr**, **Y-Bu** and **Y-Hex** (Scheme 1), in which we substituted the fluorine atoms in the 2-(3-oxo-2,3-dihydro-1*H*-inden-1-ylidene)malononitrile (IC) end groups with alkyl chains of increasing length (methyl, propyl, butyl and hexyl chains). This substitution should have multiple effects: (a) exchanging the electron-withdrawing fluorine atoms with slightly electron donating alkyl chains should lift the FMO energies of these acceptors. Implementing the alkylated acceptors as the third component to the active layer should improve the V_{OC} of the OSCs. (b) The alkyl chains should improve the solubility of the molecules in *o*-xylene. That way, we aim to process the final ternary OSCs solely from the non-halogenated *o*-xylene. (c) The alkylated acceptors should influence the packing behaviour of the ternary bulk heterojunction (BHJ). Suppressing over-aggregation of **PM6:DTY6** should retain or potentially improve the FF and J_{SC}.

After the preparation of the acceptors and their thorough characterization, we investigated the performance of each acceptor in a ternary setup with **PM6:DTY6**. By balancing the effect of the side chain length on the solubility and packing behaviour of the active layer, we aimed to find the optimal materials and parameter combinations for efficient ternary OSCs processed from non-halogenated solvents. From correlating the OSC performance with morphological investigations, we derived structure–property relationships for the investigated ternary systems.

Results and discussion

Synthesis and characterization

The four acceptors (Scheme 1) were obtained from Knoevenagel condensations of the commercially available Y6 core dialdehyde with corresponding di-alkylated end groups 2-(5,6-dialkyl-3-oxo-2,3-dihydro-1*H*-inden-1-ylidene)malononitrile (2RIC). The 2RIC end groups were synthesized in a 5-step reaction route (Scheme 2). This sequence started with an alkylation of the starting material 2,3-dimethyl-1,3-butadiene (**1**) with the respective alkyl bromide to obtain the propyl, butyl and hexyl chain lengths. The alkylation was followed by a pericyclic Diels–Alder reaction of the respective 1,3-butadienes (**1**, **3b–d**) with dimethyl acetylenedicarboxylate to form the corresponding cyclohexa-1,4-dienes (**4a–d**), which were then oxidized with

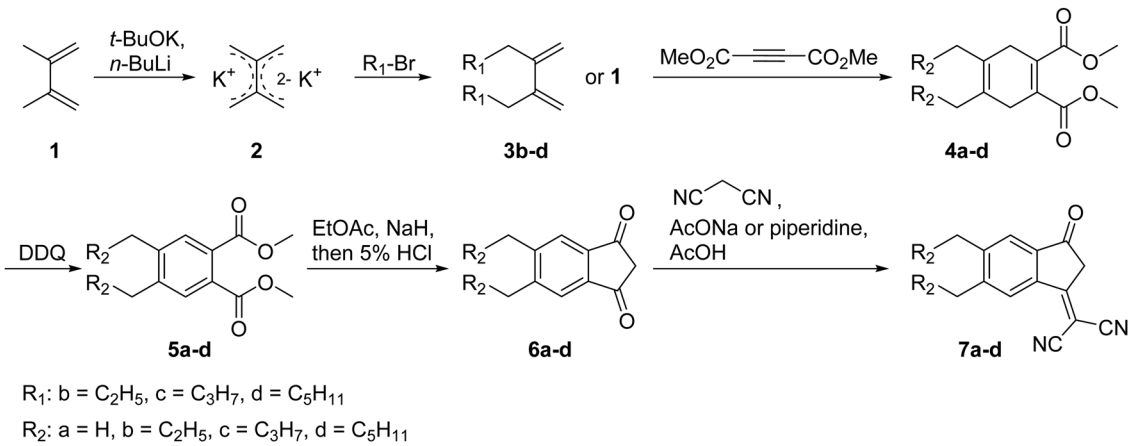

Scheme 2 Synthetic route towards the di-alkylated end groups 2RIC (**7a–d**).

© 2023 The Author(s). Published by the Royal Society of Chemistry

Open Access Article. Published on 01 2023. Downloaded on 29/07/25 02:51:43.
This article is licensed under a Creative Commons Attribution 3.0 Unported Licence.

Table 1 Optical and electrochemical properties of the novel acceptors

Compound	$\lambda_{max}^{sol,abs}$ (nm)	$\lambda_{max}^{tf,abs}$ (nm)	$\lambda_{max}^{sol,em}$ (nm)	ε_{sol} (10^5 M^{-1} cm^{-1})	$E_g^{sol\,a}$ (eV)	$E_g^{tf\,b}$ (eV)	$E_g^{CV\,c}$ (eV)	HOMO/LUMO (eV)	$T_{dec}{}^{d}$ (°C)
Y-Me	708	774	753	1.7	1.70	1.44	1.82	−5.52/−3.70	352
Y-Pr	710	767	753	2.0	1.69	1.47	1.78	−5.50/−3.72	339
Y-Bu	710	764	754	1.9	1.69	1.49	1.83	−5.54/−3.71	342
Y-Hex	710	765	754	2.0	1.69	1.49	1.87	−5.57/−3.69	346

[a] Optical gaps in chloroform, determined from the intersection of absorption and emission spectra. [b] Bandgaps of thin films, determined from the absorption onset tangent. [c] Electrochemical gaps, determined from cyclic voltammetry measurements of thin films. [d] Decomposition onset temperatures (determined at 5% weight loss).

2,3-dichloro-5,6-dicyano-1,4-benzoquinone DDQ to the substituted benzenes in the form of their dimethyl phthalates (**5a–d**). The phthalates were then converted in two remaining steps to, first, their respective indan-1,3-diones (**6a–d**) by carbon dioxide cleavage, and second, the final end groups (**7a–d**) by a base-catalyzed Knoevenagel condensation with malononitrile. The full preparation and characterization details are shown in the ESI.†

The optical properties of the acceptors were measured by UV-Vis absorption and fluorescence spectroscopy in solution. The characteristic values are summarized in Table 1. All four acceptors exhibit identical absorption and emission properties in chloroform (Fig. 1(a)). The acceptors have absorption maxima at 708–710 nm, and absorption onsets at 756 nm, combined with high absorption coefficients of 1.7–2.0 × 10^5 M^{-1} cm^{-1}. Compared to **DTY6**, all acceptors exhibit blue-shifted spectra, which was expected when removing the electron withdrawing fluorine atoms. The UV-Vis spectra in *o*-xylene and chlorobenzene exhibit similar properties (Fig. S1, ESI†). In thin films (Fig. 1(b)), the absorbance spectra indicate different aggregation behaviours for the acceptors caused by the different side chain lengths. The absorption maxima and onsets show increasing bathochromic shifts with decreasing side chain lengths, with the strongest shifted absorption onset for **Y-Me** at 861 nm. The large shift of 105 nm of the absorption onset indicates that **Y-Me** tends to aggregate stronger than the other acceptors. Additionally, the four acceptors exhibit different relative intensities of the two shoulder absorption peaks located at 688 nm and 624 nm, respectively. According to DFT calculations done by Zou *et al.* for Y6 in chloroform, the peak at 624 nm corresponds to the electronic $S_0 \rightarrow S_2$ excitation, whereas the shoulder at 688 nm corresponds to the excitation to the first vibration band (0−1) of the $S_0 \rightarrow S_1$ excitation.[23] In general, all acceptors show an increased relative contribution of both peaks compared to the solution spectra. Additionally, the long-chained acceptors (**Y-Bu** and **Y-Hex**) exhibit stronger relative intensities of the $S_0 \rightarrow S_2$ peaks (624 nm) compared to the short-chained acceptors (**Y-Me** and **Y-Pr**).

To quantify the changes of the molecules' electrochemical properties, we conducted cyclic voltammetry measurements (Fig. 1(c) and Fig. S2, ESI†). All four acceptors exhibit similar energy values for the highest occupied molecular orbital (HOMO) and the lowest unoccupied molecular orbital (LUMO, Table 1). The levels for the HOMO/LUMO are −5.52/−3.70 eV (**Y-Me**), −5.50/−3.72 eV (**Y-Pr**), −5.54/−3.71 eV (**Y-Bu**), and −5.57/−3.69 eV (**Y-Hex**), respectively. Compared to **DTY6** (HOMO/LUMO 5.75/3.85 eV), the HOMO and the LUMO energies of all four acceptors are shifted upwards by approx. 0.20 eV and 0.15 eV, respectively. These shifts fit well with the expected change when removing the electron withdrawing fluorine from the IC end groups. When comparing the energy offsets between the acceptors and **PM6**, as well as **DTY6**, we achieved the desired energy level cascade necessary for efficient ternary OSCs. Including our acceptors as a third component to **PM6:DTY6** should improve the V_{OC} of the ternary OSCs caused by the upshifted LUMO energies.

To examine the thermal properties, we conducted thermogravimetry measurements (Fig. S3, ESI†). All four acceptors exhibit high thermal stabilities, with constant weights up to 330–350 °C (Table 1), where thermal decomposition starts.

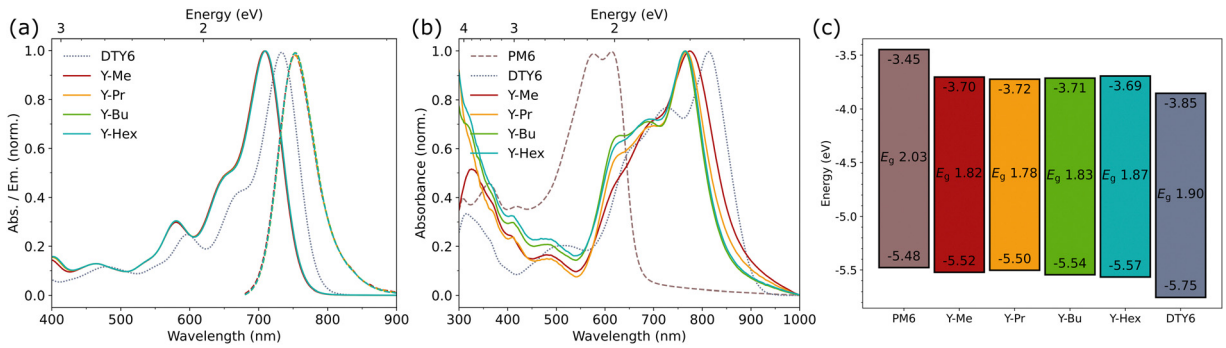

Fig. 1 (a) UV-Vis absorbance (solid lines) and emission (dashed lines) spectra in chloroform. (b) UV-Vis spectra of thin films. (c) Frontier molecular orbital energies and electrochemical bandgaps (E_g) determined from cyclic voltammetry measurements.

Open Access Article. Published on 01 2023. Downloaded on 29/07/25 02:51:43.
This article is licensed under a Creative Commons Attribution 3.0 Unported Licence.

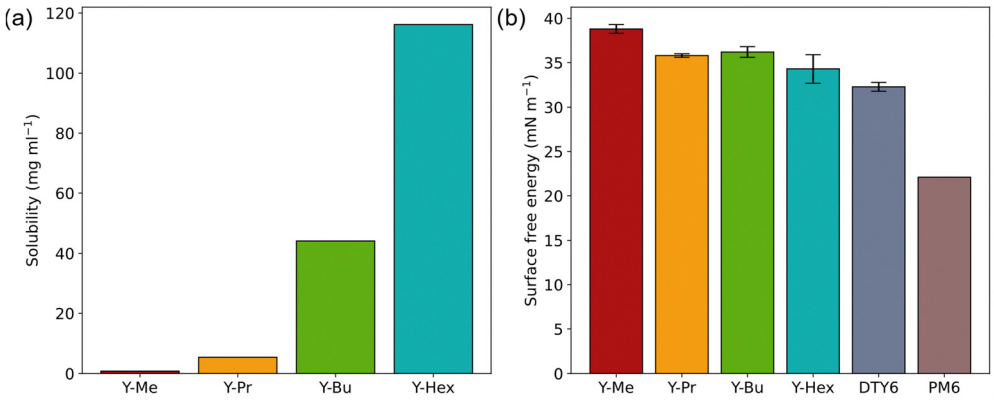

Fig. 2 (a) Solubilities of the acceptors in *o*-xylene at room temperature. (b) Surface free energy trends of the ternary setup components.

Compared to Y6 as a di-fluorinated reference, which has a reported decomposition temperature of 318 °C, the substitution of the fluorines by alkyl groups improves the thermal stability of the acceptors.[24]

Moreover, the solubilities of the acceptors exhibit a strong dependency on the chain length in the desired processing solvent *o*-xylene (Fig. 2(a)). **Y-Me** exhibits the lowest solubility (1 mg ml^{-1}), which then increases nonlinearly for **Y-Pr** (5 mg ml^{-1}), **Y-Bu** (44 mg ml^{-1}), and **Y-Hex** (116 mg ml^{-1}). Since precursor solutions for OSCs typically have total concentrations in the range of 10–20 mg ml^{-1}, all acceptors except **Y-Me** seem to fit well for processing from *o*-xylene. However, since the second acceptor in the ternary solar cell setup is only added in small amounts, **Y-Me** could also be used. Additionally, the interaction of the alkylated acceptors with **DTY6** could improve their overall solubility.

To check if the synthesized acceptors exhibit desirable interaction properties with both **PM6** and **DTY6**, we determined the surface free energies (SFEs) of all components from contact angle measurements (Fig. S5–S9, ESI†). The SFE values were determined with the method of Owens–Wendt–Rabel–Kaelble (OWRK)[25] and Wu[26] (Table 2 and Fig. 2(b)). Of all acceptors, **Y-Me** exhibits the highest SFE (38.8 ± 0.5 mN m^{-1}). The remaining three acceptors **Y-Pr**, **Y-Bu**, and **Y-Hex** have similar values (35.8 ± 0.2 mN m^{-1}, 36.2 ± 0.6 mN m^{-1}, and 34.3 ± 1.6 mN m^{-1}, respectively). **DTY6** exhibits a slightly reduced SFE (32.3 ± 0.5 mN m^{-1}), followed by a low value for **PM6** (22.1 mN m^{-1}). We further calculated the Flory–Huggins interaction parameters for the material combinations present in the desired ternary blends (Table 3). All acceptors exhibit interaction parameters with **DTY6** nearing zero. The low values indicate that **DTY6** should be fully miscible with all alkylated acceptors, even **Y-Me**. The interaction parameters with **PM6** are the lowest for **PM6:DTY6** (0.96), indicating the best blending behaviour. For the acceptors, the interaction parameters are in the range of 1.3–2.3. All values indicate that the acceptors should interact well with both **PM6** and **DTY6** in the desired ternary BHJ blends.

Table 2 Surface free energy values (mN m^{-1}) with their dispersive and polar part

Compound	SFE	Dispersive	Polar
Y-Me	38.8 ± 0.5	38.3 ± 0.3	0.5 ± 0.2
Y-Pr	35.8 ± 0.2	35.2 ± 0.2	0.6 ± 0.1
Y-Bu	36.2 ± 0.6	35.5 ± 0.5	0.7 ± 0.1
Y-Hex	34.3 ± 1.6	32.4 ± 1.3	1.9 ± 0.4
DTY6	32.3 ± 0.5	32.1 ± 0.5	0.1 ± 0.1
PM6	22.1	16.8	5.3

Table 3 Flory–Huggins interaction parameters of donor and acceptor combinations present in the ternary blends

Compound	**DTY6**	**PM6**
Y-Me	0.31	2.34
Y-Pr	0.09	1.65
Y-Bu	0.12	1.74
Y-Hex	0.03	1.35
DTY6	—	0.96

Solar cell characterization

We tested all four acceptors in both a binary (with **PM6** and PBDB-T as donor polymers, respectively) and a ternary setup (with **PM6:DTY6** as the main components of the active layer). Both the binary and ternary setups were built using the same conventional architecture, namely ITO/PEDOT:PSS/BHJ/PNDIT-F3N-Br/Ag. The binary OSCs based on **PM6:A** (where **A** is **Y-Me**, **Y-Pr**, **Y-Bu**, and **Y-Hex**, respectively) achieved consistently low efficiencies (Fig. S10a and Table S1, ESI†). The unusually low PCEs of 0.2–1.3% can be explained by the bad match of the HOMO levels of **PM6** with the acceptors. The elevated HOMO energies of the alkylated acceptors lead to an insufficient energy offset, resulting in poor exciton dissociation and charge transfer. Identical results were obtained by Zhan *et al.*, when they combined the similar mono-alkylated BTP-M with **PM6**.[22] The same setup with PBDB-T as a donor, which exhibits a higher HOMO level than **PM6**, achieved significantly higher efficiencies (Fig. S10b and Table S1, ESI†). However, with PCEs of 4–7%, the acceptors still show suboptimal efficiencies when used as the sole acceptor in binary OSCs. This could be due to a combined effect of low orbital energy offset with PBDB-T, and a

© 2023 The Author(s). Published by the Royal Society of Chemistry

Open Access Article. Published on 01 2023. Downloaded on 29/07/25 02:51:43.
This article is licensed under a Creative Commons Attribution 3.0 Unported Licence.

Table 4 Summary of OSC data

BHJ	A content[a] (wt%)	V_{OC} (V)	J_{SC} (mA cm^{-2})	FF (%)	PCE (%)	k^c (1)	n^d ($k_BT\,q^{-1}$)	η_{diss} (%)	η_{cc} (%)	$J_{SC}^{EQE\,e}$ (mA cm^{-2})
PM6:DTY6:Y-Me	15	0.87 ± 0.01 (0.87)	22.5 ± 0.4 (24.2)	72 ± 1 (74)	14.1 ± 0.2 (15.7)[b]	0.93	1.1	99	90	22.9
PM6:DTY6:Y-Pr	20	0.87 ± 0.01 (0.87)	23.3 ± 0.2 (24.0)	66 ± 1 (66)	13.4 ± 0.1 (13.8)	0.93	1.3	99	86	23.1
PM6:DTY6:Y-Bu	20	0.87 ± 0.01 (0.87)	22.7 ± 0.2 (23.6)	69 ± 1 (70)	13.5 ± 0.1 (14.4)	0.93	1.1	98	86	22.2
PM6:DTY6:Y-Hex	20	0.87 ± 0.01 (0.87)	22.5 ± 0.3 (23.8)	69 ± 1 (71)	13.5 ± 0.2 (14.6)	0.93	1.2	99	87	21.4
PM6:DTY6	0	0.81 ± 0.01 (0.81)	23.5 ± 0.4 (24.6)	70 ± 1 (70)	13.3 ± 0.2 (14.1)	0.92	1.2	99	87	22.9

[a] Relative amount of the second acceptor respective to the total acceptor amount. The overall D/A ratio for all OSCs is 1/1.2. [b] Arithmetic means and standard errors calculated from 10 cells; top values in parentheses. [c] Slope of the light intensity dependence fit of the J_{SC}. [d] Ideality factor, calculated from the slope of the light intensity dependence fit of the V_{OC}. [e] Obtained from the integrated EQE spectra.

reduced intramolecular charge transfer strength of the acceptors caused by the removal of the electron withdrawing fluorine atoms.

The ternary OSCs achieved greatly improved efficiencies compared to the binary OSCs. The performances of the ternary devices are summarized in Table 4 and Fig. 3. As intended, the addition of our acceptors to **PM6:DTY6** resulted in improved values for the V_{OC}. The highest efficiencies were obtained with 15 wt.% of **Y-Me** (OSC data with varied contents see Table S2, ESI†) and 20 wt% of **Y-Pr**, **Y-Bu**, and **Y-Hex**, respectively. For all four ternary systems, the V_{OC} was increased by 0.06 V from 0.81 ± 0.01 V (binary reference OSCs with **PM6:DTY6**) to 0.87 ± 0.01 V (ternary OSCs). This improvement can be rationalized by the larger FMO energy offset between **PM6** and the alkylated acceptors (*cf.* Fig. 1(c)). Interestingly, using a lower relative amount of **Y-Me** (15 wt%) yielded an equally high V_{OC} increase as using **Y-Pr**, **Y-Bu**, and **Y-Hex** in higher amounts (20 wt%). Since all alkylated acceptors exhibit identical LUMO energies, also other factors seem to come to play. According to a relationship derived by Garcia–Belmonte, the V_{OC} is not only dependent on the energy offset of the HOMO of the donor and the LUMO of the acceptors (specifically, the respective maxima of their Gaussian density-of-state (DOS) distributions) but also dependent on the standard deviations of their DOS distributions.[27] The equal V_{OC} increase of the **Y-Me** based OSCs could therefore be explained by a narrower DOS distribution, which in turn is indicative of a higher-ordered absorber layer of the **Y-Me** based OSCs compared to the other ternary OSCs.

With the improvement of the V_{OC} values, combined with similar values for the J_{SC} (22.5–23.3 mA cm^{-2}) and for the FF (66–72%) compared to the binary setup, the ternary OSCs achieved improved efficiencies. While the ternary OSCs with **Y-Pr** (PCE 13.4 ± 0.1%), **Y-Bu** (PCE 13.5 ± 0.1%) and **Y-Hex** (PCE 13.5 ± 0.2%) as the third component yielded slightly higher

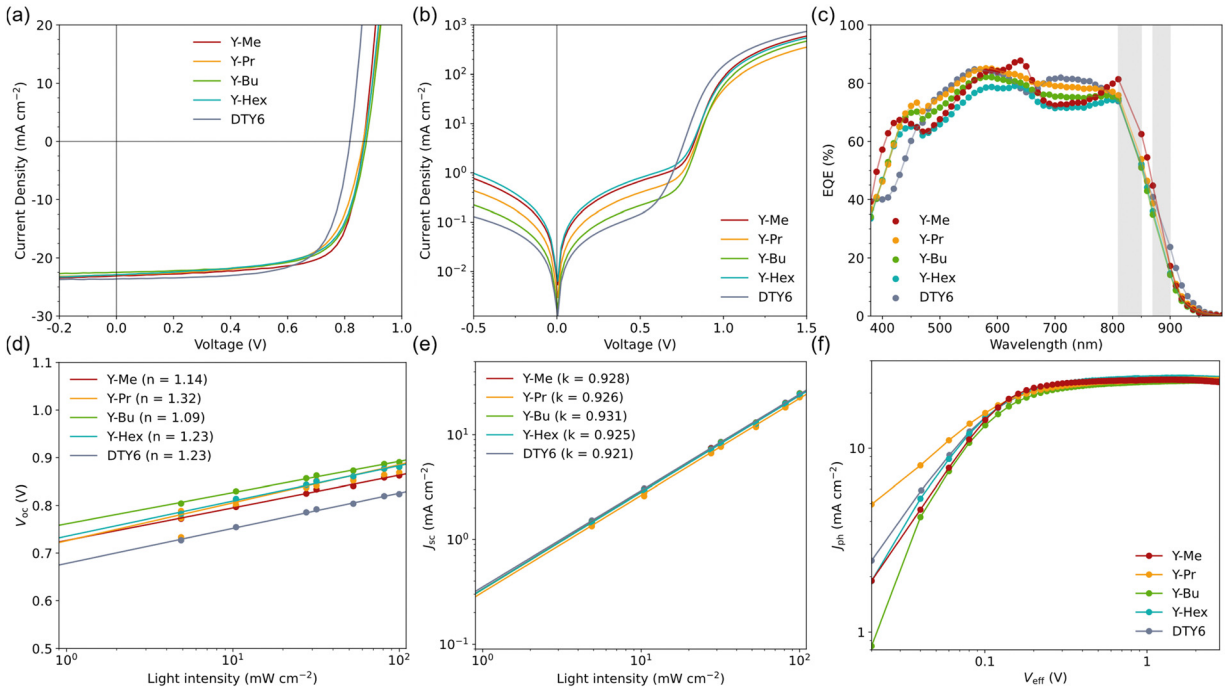

Fig. 3 Solar cell characterization of the optimized ternary OSC setups (**PM6**:**DTY6**:**A**, where **A** is **Y-Me**, **Y-Pr**, **Y-Bu**, and **Y-Hex**, respectively, labelled by "**A**") and the binary reference system (**PM6**:**DTY6**, labelled "**DTY6**"). (a) JV curves under illuminated (AM1.5G) conditions. (b) Dark JV curves in semilog-depiction. (c) EQE spectra (data points in the grey shaded areas were removed because of emission spikes of the xenon lamp). (d) Light intensity dependences of the V_{OC} with linear fits and ideality factors n. (e) Light intensity dependences of the J_{SC} with linear fits and slope values. (f) J_{ph}–V_{eff} curves.

Open Access Article. Published on 01 2023. Downloaded on 29/07/25 02:51:43.
This article is licensed under a Creative Commons Attribution 3.0 Unported Licence.

PCEs than the binary reference (PCE 13.3 ± 0.2%), the greatest improvement was achieved with **Y-Me** (PCE 14.1 ± 0.2%). The **PM6:DTY6:Y-Me** OSCs showed the highest FF (72 ± 1%) combined with the improved V_{OC}, resulting in an increased average PCE by 0.8 percentage points.

The external quantum efficiency (EQE) spectra (Fig. 3(c)) show similar behaviour for all ternary and binary OSCs. All measurements show good agreement of the integrated J_{SC}^{EQE} and the experimental J_{SC} values (Table 4). The spectra exhibit a broad wavelength interval of efficient photocurrent generation, with constant EQE values in the range of 60–85%. All ternary OSCs exhibit a higher contribution at low wavelengths (400–500 nm), which can be explained by the stronger light absorption of the alkylated acceptors in this interval compared to **DTY6** (*cf.* Fig. 1(b)). From 700–800 nm, the ternary OSCs, but especially those with **Y-Me** and **Y-Hex**, exhibit a small valley. Since all acceptors, as well as **DTY6**, have strong light absorption in this interval (*cf.* Fig. 1(b)), the cause of the valleys seems to be a different step of the charge generation process (namely exciton diffusion, exciton dissociation, charge transport, or charge collection[28,29]).

For more detail on the recombination mechanisms, we measured the light intensity dependences of the J_{SC} and V_{OC} for all systems (*JV* curves see Fig. S11, ESI†). The V_{OC} dependences (Fig. 3(d)) show identical trends for both the ternary and binary OSCs. From the slopes of the linear fits, we calculated the ideality factors n of the OSCs (Table 4).[30] All systems exhibit values for n of 1.1–1.3. The proximity to 1 indicates that direct/bimolecular recombination (n = 1) dominates at open-circuit conditions and that the rate of undesired trap-assisted recombination (n = 2) is negligible. The largest difference between the ternary and binary setups lies less in the recombination properties, but in the absolute values of the V_{OC} for all measured light intensities. The ternary OSCs achieve consistently higher V_{OC} values than the binary reference. This underlines the advantageous effect of adding our acceptors as the third component in a ternary setup. The J_{SC} dependences (Fig. 3(e)) show almost identical behaviour for all tested systems. Similar to the V_{OC} trends, the slopes k of the linear fits can be used to make statements about the recombination properties (Table 4).[31] The values for k of 0.92–0.93 indicate that all solar cells exhibit a negligible ratio of bimolecular recombination at short-circuit conditions.

Moreover, we measured the dependence of the photocurrent density J_{ph} on the effective voltage V_{eff} for all setups. J_{ph} is defined as the difference of the illuminated and dark current densities ($J_{ph} = J_{light} - J_{dark}$), and V_{eff} is defined as $V_0 - V_{appl}$, where V_0 is the voltage where J_{ph} is zero, and V_{appl} is the applied voltage.[32–34] The obtained J_{ph}–V_{eff} curves (Fig. 3(f)) exhibit the greatest variation in the lower V_{eff} interval ($0 < V_{eff} < 0.1$ V), which corresponds to the interval of the *JV* curve just below V_0. These variations stem from different values of the FF and series resistances of the *JV* curves (shunt and series resistances see Table S3, ESI†). At the higher V_{eff} interval, which corresponds to the fourth quadrant of the *JV* curves, all setups again behave similarly.

From the J_{ph}–V_{eff} trends, we calculated the exciton dissociation efficiencies (η_{diss}) as the ratio of the J_{ph} at short-circuit conditions compared to J_{ph} at V_{eff} = 2.0 V, as well as the charge collection efficiencies (η_{cc}) as the ratio of the J_{ph} at maximum-power-point conditions compared to J_{ph} at V_{eff} = 2.0 V (Table 4). While η_{diss} is equally high for all OSCs (in the range of 98–99%), the η_{cc} has a distinctly high value of 90% for the **Y-Me** based ternary OSCs. Compared to the other setups, which exhibit similar values of 86–87%, this elevation indicates that **Y-Me** has a positive effect on the charge collection efficiency in the BHJ. This result agrees with the higher FF of the **Y-Me** based ternary system. These better values for the **Y-Me** based OSCs could be explained by a stronger, apparently beneficial, influence of **Y-Me** on the BHJ morphology and crystallinity compared to the acceptors with longer alkyl chains at the end groups, which is discussed in more detail in the morphology investigation section.

All four acceptors yielded ternary OSCs with attractive properties. By consistently improving the V_{OC} of all ternary setups, while simultaneously maintaining all other properties similar to the already well-performing binary reference setup **PM6:DTY6**, all systems revealed improved PCEs. Interestingly, despite low values for the solubility in *o*-xylene, **Y-Me** achieved the greatest PCE improvement of all ternary systems. To investigate the reason for this controversial trend, we further conducted morphological characterizations with all ternary absorber layer blends.

Morphological investigation

For determining the surface morphologies, we conducted atomic force microscopy (AFM) measurements (Fig. 4 and Fig. S12, S13, ESI†). The height images reveal that the ternary **PM6:DTY6:Y-Me** blend shows well-visible elongated fibrillar structures at the surface, while no pronounced fibrillar structures are recognized in the **PM6:DTY6** binary blend. The same elongated structures are also visible in the ternary **PM6:DTY6:Y-Pr** blend, but less defined. Going to longer chained acceptors (ternary blends with **Y-Bu** and **Y-Hex**), the fibrillar structures gradually weaken. The presence of fibrils in the ternary **Y-Me** blend could explain the improved FF of the OSCs, since fibrillar structures in Y-series OSCs are literature-known to yield high-performing OSCs.[4,35–37] We argue that through the elongated side chains in the centre of **DTY6**, their solubility in *o*-xylene is improved, but on the downside, the side chains seem to suppress the beneficial crystallization tendency that produces these fibrillar structures. The addition of **Y-Me**, which tends to strong aggregation and crystallization, seems to promote this beneficial self-assembly, even if only added in low amounts (15 wt%).

We further conducted grazing-incidence wide-angle X-ray scattering measurements (GIWAXS) of the blend films to further investigate their crystallinity and molecular packing. The diffraction patterns of the pristine acceptor films (2D images see Fig. S15 (ESI†), 1D line cuts see Fig. 5(b) and Fig. S16, ESI†) reveal a strong difference for **Y-Me**, which exhibits strong crystalline features. In contrast, **Y-Pr**, **Y-Bu**

© 2023 The Author(s). Published by the Royal Society of Chemistry

Open Access Article. Published on 01 2023. Downloaded on 29/07/25 02:51:43.
This article is licensed under a Creative Commons Attribution 3.0 Unported Licence.

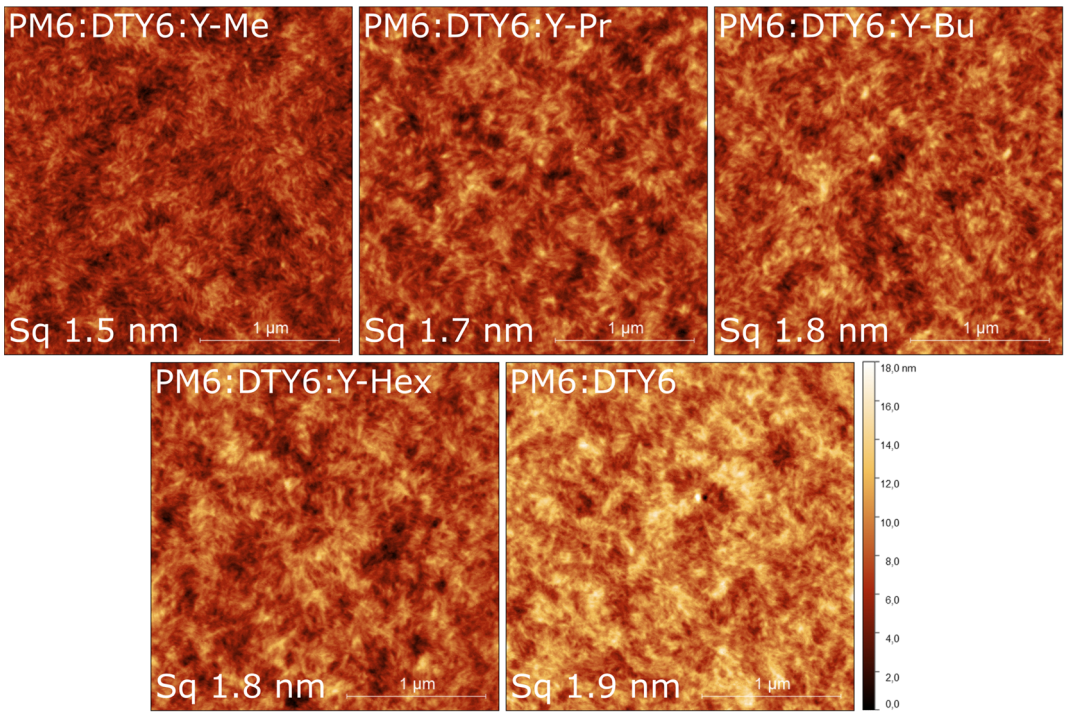

Fig. 4 AFM height images (2.5 × 2.5 μm^2) of the active layers of the ternary and binary blends prepared on glass/ITO/PEDOT:PSS substrates. The corresponding phase images are shown in Fig. S12 (ESI†).

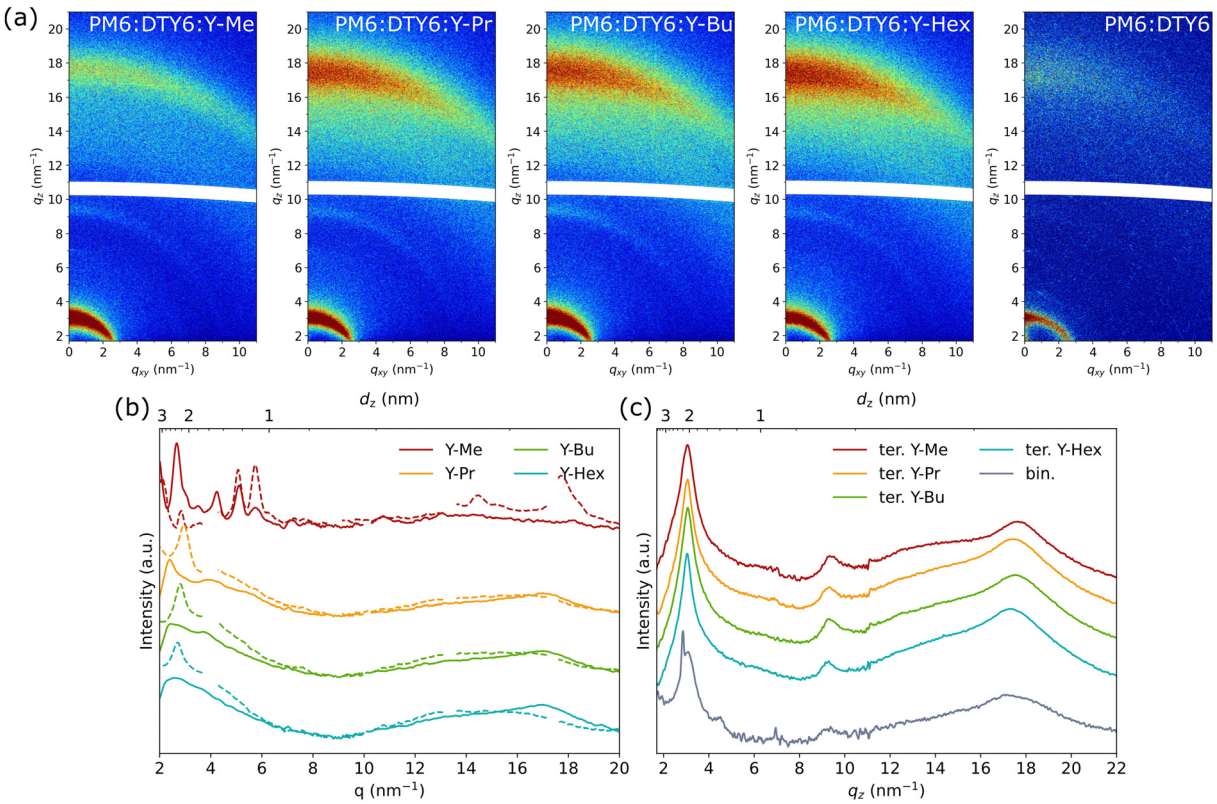

Fig. 5 GIWAXS characterization of drop cast films with thermal annealing treatment at 100 °C for 10 min. (a) 2D GIWAXS images of the ternary and binary donor:acceptor blends. 1D line cuts of (b) the neat acceptor films (in-plane (q_{xy}) solid lines, out-of-plane (q_z) dashed lines), and (c) the ternary and binary donor:acceptor blends (q_z direction). The line cuts are shifted vertically for better visibility.

Open Access Article. Published on 01 2023. Downloaded on 29/07/25 02:51:43.
This article is licensed under a Creative Commons Attribution 3.0 Unported Licence.

and **Y-Hex** are similar to each other, showing less pronounced attributes in the line cuts, in both the in-plane (IP) and out-of-plane (OOP) direction. Moreover, **Y-Me** adopts a distinct face-on orientation, as indicated by the OOP-oriented π–π stacking peak at 17.7 nm^{-1} (0.35 nm). The remaining three acceptors **Y-Pr**, **Y-Bu** and **Y-Hex** exhibit a preferential edge-on orientation, apparent from the IP-oriented π–π stacking peaks. Additionally, the π–π stacking distances are slightly increased for all three acceptors with longer alkyl chains, giving signals at q_{xy} = 17.0 nm^{-1} (0.37 nm). The pristine **PM6** film (Fig. S16b, ESI†) exhibits a preferred face-on orientation, with the π–π stacking signal at q_z = 16.5 nm^{-1} (0.38 nm) and a lamellar stacking signal at 3.15 nm^{-1} (2.0 nm).

The ternary blends (Fig. 5(a) and (c)) exhibit more similar GIWAXS patterns clearly featuring the polymer-specific signals, namely the π–π stacking signal as well as a distinct OOP signal at 9.3 nm^{-1} (0.68 nm). This means that **PM6** retains its preferential face-on orientation in the ternary blends as well as the binary **PM6**:**DTY6** film. The π–π stacking signal of the blends exhibits slightly increasing stacking distances upon increasing the side chain lengths of the end group alkylated acceptor. The same was observed for the pristine acceptor films. The peak positions for the ternary blends are at 17.7 nm^{-1} (0.35 nm) for **Y-Me**, at 17.4 nm^{-1} (0.36 nm) for **Y-Pr**, at 17.5 nm^{-1} (0.36 nm) for **Y-Bu**, and at 17.4 nm^{-1} (0.36 nm) for **Y-Hex**. In comparison, the π–π stacking signal of the binary blend **PM6**:**DTY6** is observed at 17.1 nm^{-1} revealing the highest π–π stacking distance (0.37 nm) in this series. Overall, the alkylated acceptors (**Y-Me**, **Y-Pr**, **Y-Bu**, and **Y-Hex**) and **DTY6** both adopt a face-on orientation in the ternary blends.

At higher length-scales, all four ternary blends show a pronounced and broad lamellar stacking peak in the q_z direction at 3.05–3.07 nm^{-1} (2.05–2.06 nm). This position fits well with the intense lamellar stacking peak of the pristine **PM6** film (Fig. S16b, ESI†), located at q_z = 3.15 nm^{-1} (2.0 nm). So, the lamellar signals of the ternary blends are a superposition of all lamellar donor and acceptor signals. Merely in the binary **PM6**:**DTY6** blend, the lamellar stacking signals of the donor and acceptor appear separated, with the **PM6** signal at q_z = 3.10 nm^{-1} (2.03 nm) and a sharp **DTY6** signal at q_z = 2.85 nm^{-1} (2.20 nm). The absence of this sharp signal in the ternary blends suggests that the alkylated acceptors partly disrupt the long-range crystallization of **DTY6**. This is likely because **DTY6** and the alkylated acceptors form well-mixed blends according to the low Flory–Huggins interaction parameters, and thus reduce the amount of pure crystalline **DTY6** domains.

Comparing the results of the AFM and GIWAXS characterizations, the crystalline domains of the four ternary blends appear relatively similar. Of all alkylated acceptors, **Y-Me** exhibits the smallest π–π stacking distance in the blend. In all cases, adding the alkylated acceptors as a third component seems to slightly reduce the order of the **DTY6** lamellar stacking. On a larger scale, the alkylated acceptors improve the formation of beneficial fibrillar structures, with the most defined structures for the **Y-Me** based blend.

Conclusions

In this work, we chose **PM6**:**DTY6** as a model material system because of its high performance and good processability from non-halogenated solvents. By adding a second acceptor, we aimed to improve the V_{OC} and consequently the PCE of the resulting ternary solar cells. For this, we prepared four Y-series acceptors **Y-Me**, **Y-Pr**, **Y-Bu** and **Y-Hex**, in which the fluorine atoms on the IC terminals are substituted with alkyl side chains of increasing lengths. The alkylation resulted in elevated frontier molecular orbital energies, which created the necessary energy level cascade compared to **PM6** and **DTY6** for efficient ternary solar cells. Furthermore, the longer-chained acceptors show high solubilities in the non-halogenated solvent *o*-xylene and promise good miscibilities with both **PM6** and **DTY6**, as indicated from the low Flory–Huggins interaction parameters.

The acceptors were incorporated in ternary solar cells with **PM6** and **DTY6** (**PM6**:**DTY6**:**A**, where **A** is **Y-Me**, **Y-Pr**, **Y-Bu**, and **Y-Hex**, respectively), processed solely from *o*-xylene. All ternary solar cells exhibit improved open-circuit voltages (from 0.81 V for the binary reference to 0.87 V for all four ternary systems), which stems from the higher energy difference between the HOMO of **PM6** and the LUMO of the alkylated acceptors. Combined with similar values for the FF and J_{SC}, the addition of the alkylated acceptors resulted in improved efficiencies for all resulting ternary solar cells. With average power conversion efficiencies of 14.1% (**Y-Me**), 13.4% (**Y-Pr**), 13.5% (**Y-Bu**) and 13.5% (**Y-Hex**), the **Y-Me** based ternary OSCs achieved the greatest improvement compared to 13.3% for the binary reference (**PM6**:**DTY6**). An investigation of the morphological properties revealed that the alkylated acceptors as a third component facilitate the formation of a fibrillar morphology (strongest with **Y-Me**, successively less pronounced for **Y-Pr**, **Y-Bu**, and **Y-Hex**), which is often observed in the literature in high-performing solar cells. Furthermore, by adding the different alkylated acceptors to the **PM6**:**DTY6** blends, the crystallinity and packing behaviour of **DTY6** could be tailored.

Our findings reveal that the addition of the investigated alkylated acceptors is a convenient method to increase the control over the electronic and morphological properties of the **PM6**:**DTY6** model absorber layer system, which can potentially be applied to a variety of active layer systems to increase their efficiency.

Experimental

The full methodology, synthetic routes and characterizations are included in the ESI.†

Author contributions

P. F.: conceptualization, data curation, formal analysis, investigation (synthesis, structural analysis, physical characterization, solar cell characterization, morphological characterization), methodology, project administration, supervision, visualization, writing – original draft, writing – review & editing. D. P.: data curation,

© 2023 The Author(s). Published by the Royal Society of Chemistry

Open Access Article. Published on 01 2023. Downloaded on 29/07/25 02:51:43.
This article is licensed under a Creative Commons Attribution 3.0 Unported Licence.

investigation (physical characterization, solar cell characterization), writing – review & editing. I. K.: conceptualization, project administration, investigation (synthesis, structural characterization), supervision, writing – review & editing. A. S.: investigation (synthesis, structural characterization), writing – original draft, writing – review & editing. K. B.: conceptualization, project administration, investigation (synthesis, structural characterization), supervision, writing – review & editing. M. R.: conceptualization, project administration, writing – review & editing. J. B. S.: investigation (AFM), writing – review & editing. H. A.: investigation (GIWAXS), resources, writing – review & editing. T. R.: conceptualization, funding acquisition, project administration, supervision, writing – review & editing. G. T.: funding acquisition, supervision, resources, writing – review & editing.

Conflicts of interest

There are no conflicts to declare.

Acknowledgements

Financial support is gratefully acknowledged from the Zukunftsfonds Steiermark and the Klimafonds Graz (project GreenOPVSolutions). Moreover, the authors would like to acknowledge the use of the Somapp Lab, a core facility supported by the Austrian Federal Ministry of Education, Science and Research, the Graz University of Technology, the University of Graz and Anton Paar GmbH. The authors also acknowledge the CERIC-ERIC Consortium for the access to experimental facilities (Austrian SAXS beamline at Elettra Sincrotrone Trieste) and financial support. The authors further thank Petra Kaschnitz, Karin Bartl, and Philipp Materna for their experimental support.

Notes and references

1 H. Yao and J. Hou, *Angew. Chem., Int. Ed.*, 2022, **61**, e202209021.
2 A. Armin, W. Li, O. J. Sandberg, Z. Xiao, L. Ding, J. Nelson, D. Neher, K. Vandewal, S. Shoaee, T. Wang, H. Ade, T. Heumüller, C. Brabec and P. Meredith, *Adv. Energy Mater.*, 2021, **11**, 2003570.
3 B. Schweda, M. Reinfelds, P. Hofstadler, G. Trimmel and T. Rath, *ACS Appl. Energy Mater.*, 2021, **4**, 11899–11981.
4 L. Zhu, M. Zhang, J. Xu, C. Li, J. Yan, G. Zhou, W. Zhong, T. Hao, J. Song, X. Xue, Z. Zhou, R. Zeng, H. Zhu, C.-C. Chen, R. C. I. MacKenzie, Y. Zou, J. Nelson, Y. Zhang, Y. Sun and F. Liu, *Nat. Mater.*, 2022, **21**, 656–663.
5 C. He, Y. Pan, Y. Ouyang, Q. Shen, Y. Gao, K. Yan, J. Fang, Y. Chen, C.-Q. Ma, J. Min, C. Zhang, L. Zuo and H. Chen, *Energy Environ. Sci.*, 2022, **15**, 2537–2544.
6 X. Xu, W. Jing, H. Meng, Y. Guo, L. Yu, R. Li and Q. Peng, *Adv. Mater.*, 2023, **35**, 2208997.
7 Z. Ma, B. Zhao, Y. Gong, J. Deng and Z. Tan, *J. Mater. Chem. A*, 2019, **7**, 22826–22847.
8 S. Zhang, L. Ye, H. Zhang and J. Hou, *Mater. Today*, 2016, **19**, 533–543.
9 H. Gaspar, G. Bernardo and A. Mendes, *Nanoenergy Adv.*, 2022, **2**, 1–28.
10 S. Dong, T. Jia, K. Zhang, J. Jing and F. Huang, *Joule*, 2020, **4**, 2004–2016.
11 S. Li, C.-Z. Li, M. Shi and H. Chen, *ACS Energy Lett.*, 2020, **5**, 1554–1567.
12 B. Lu, J. Wang, Z. Zhang, J. Wang, X. Yuan, Y. Ding, Y. Wang and Y. Yao, *Nano Select*, 2021, **2**, 2029–2039.
13 N. Y. Doumon, L. Yang and F. Rosei, *Nano Energy*, 2022, **94**, 106915.
14 N. Gasparini, A. Salleo, I. McCulloch and D. Baran, *Nat. Rev. Mater.*, 2019, **4**, 229–242.
15 J. Wan, I. Dyadishchev, R. Sun, Q. Wu, Y. Wu, M. Zhang, S. Peregudova, S. Ponomarenko, Y. Luponosov and J. Min, *J. Mater. Chem. A*, 2022, **10**, 17122–17131.
16 C. Cao, H. Lai, H. Chen, Y. Zhu, M. Pu, N. Zheng and F. He, *J. Mater. Chem. A*, 2021, **9**, 16418–16426.
17 Y. Cho, T. Kumari, S. Jeong, S. M. Lee, M. Jeong, B. Lee, J. Oh, Y. Zhang, B. Huang, L. Chen and C. Yang, *Nano Energy*, 2020, **75**, 104896.
18 M. Zhang, M. Zeng, X. Deng, Z. Zhou, X. Tan, S. Tan, B. Zhao, J. Zhang and Y. Zou, *ACS Appl. Energy Mater.*, 2021, **4**, 3480–3486.
19 A. Lan, Y. Lv, J. Zhu, H. Lu, H. Do, Z.-K. Chen, J. Zhou, H. Wang, F. Chen and E. Zhou, *ACS Energy Lett.*, 2022, **7**, 2845–2855.
20 S. Zhang, X. Ma, L. Niu, S. Y. Jeong, H. Y. Woo, Z. Zhou and F. Zhang, *Sol. RRL*, 2023, **7**, 2200957.
21 H. Zhou, L. Zhang, X. Ma, Y. Xibei, Y. Zheng, Z. Liu, X. Gao, J. Zhang, Z. Liu and F. Zhang, *J. Chem. Eng.*, 2023, **462**, 142327.
22 L. Zhan, S. Li, T.-K. Lau, Y. Cui, X. Lu, M. Shi, C.-Z. Li, H. Li, J. Hou and H. Chen, *Energy Environ. Sci.*, 2020, **13**, 635–645.
23 X. Zou, G. Wen, R. Hu, G. Dong, C. Zhang, W. Zhang, H. Huang and W. Dang, *Molecules*, 2020, **25**, 4118.
24 J. Yuan, Y. Zhang, L. Zhou, G. Zhang, H.-L. Yip, T.-K. Lau, X. Lu, C. Zhu, H. Peng, P. A. Johnson, M. Leclerc, Y. Cao, J. Ulanski, Y. Li and Y. Zou, *Joule*, 2019, **3**, 1140–1151.
25 D. K. Owens and R. C. Wendt, *J. Appl. Polym. Sci.*, 1969, **13**, 1741–1747.
26 S. Wu, *J. Polym. Sci., Part C: Polym. Symp.*, 1971, **34**, 19–30.
27 G. Garcia-Belmonte, *Sol. Energy Mater. Sol. Cells*, 2010, **94**, 2166–2169.
28 A. Moliton and J.-M. Nunzi, *Polym. Int.*, 2006, **55**, 583–600.
29 J. Yan and B. R. Saunders, *RSC Adv.*, 2014, **4**, 43286–43314.
30 L. J. A. Koster, V. D. Mihailetchi, R. Ramaker and P. W. M. Blom, *Appl. Phys. Lett.*, 2005, **86**, 123509.
31 L. J. A. Koster, V. D. Mihailetchi, H. Xie and P. W. M. Blom, *Appl. Phys. Lett.*, 2005, **87**, 203502.
32 J. Hofinger, S. Weber, F. Mayr, A. Jodlbauer, M. Reinfelds, T. Rath, G. Trimmel and M. C. Scharber, *J. Mater. Chem. A*, 2022, **10**, 2888–2906.
33 Z. Hu, L. Yang, W. Gao, J. Gao, C. Xu, X. Zhang, Z. Wang, W. Tang, C. Yang and F. Zhang, *Small*, 2020, **16**, 2000441.

© 2023 The Author(s). Published by the Royal Society of Chemistry

34 C. Xu, K. Jin, Z. Xiao, Z. Zhao, X. Ma, X. Wang, J. Li, W. Xu, S. Zhang, L. Ding and F. Zhang, *Adv. Funct. Mater.*, 2021, **31**, 2107934.
35 T. Liu, L. Huo, S. Chandrabose, K. Chen, G. Han, F. Qi, X. Meng, D. Xie, W. Ma, Y. Yi, J. M. Hodgkiss, F. Liu, J. Wang, C. Yang and Y. Sun, *Adv. Mater.*, 2018, **30**, 1707353.
36 D. Li, X. Chen, J. Cai, W. Li, M. Chen, Y. Mao, B. Du, J. A. Smith, R. C. Kilbride, M. E. O'Kane, X. Zhang, Y. Zhuang, P. Wang, H. Wang, D. Liu, R. A. L. Jones, D. G. Lidzey and T. Wang, *Sci. China: Chem.*, 2020, **63**, 1461–1468.
37 D. Li, N. Deng, Y. Fu, C. Guo, B. Zhou, L. Wang, J. Zhou, D. Liu, W. Li, K. Wang, Y. Sun and T. Wang, *Adv. Mater.*, 2023, **35**, 2208211.

Open Access Article. Published on 01 2023. Downloaded on 29/07/25 02:51:43.
This article is licensed under a Creative Commons Attribution 3.0 Unported Licence.

© 2023 The Author(s). Published by the Royal Society of Chemistry